Project 076 Improved Open Rotor Noise Prediction Capabilities

Georgia Institute of Technology

Project Lead Investigator

Principal Investigator: Professor Dimitri N. Mavris
Director, Aerospace Systems Design Laboratory
School of Aerospace Engineering, Georgia Institute of Technology
Phone: (404) 894-1557, Fax: (404) 894-6596
Email: dimitri.mavris@ae.gatech.edu

Co-Principal Investigator: Dr. Jimmy Tai
Division Chief, Propulsion & Energy
Aerospace Systems Design Laboratory
School of Aerospace Engineering, Georgia Institute of Technology
Phone: (404) 894-0197, Fax: (404) 894-6596
Email: jimmy.tai@ae.gatech.edu

University Participants

Georgia Institute of Technology (Georgia Tech)

- P.I.s: Dr. Dimitri N. Mavris, Dr. Jimmy Tai
- FAA Award Number: 13-C-AJFE-GIT-078
- Period of Performance: October 1, 2022 to March 30, 2023

Project Funding Level

The project funding is $300,000 per year from the FAA. The cost-share match amount is $300,000 per year. The sources of matching are cash and in-kind cost-share from an industry partner (GE).

Investigation Team

Dr. Dimitri Mavris, Professor, Georgia Tech (P.I.)
Dr. Jimmy Tai, Senior Research Engineer, Georgia Tech (Co-P.I.)
Dr. Miguel Walter, Research Engineer II, Georgia Tech
Mr. Brenton Willier, Graduate Student, Georgia Tech
Mr. Grant Stevenson, Graduate Student, Georgia Tech

Project Overview

The contrarotating open rotor (CROR) system has promising environmental benefits because of its ultra-high bypass ratio and high propulsive efficiency. The reduced fuel burn and emissions of the CROR compared with an equivalent-thrust turbofan make it an economically viable and environmentally friendly propulsion alternative to traditional ducted systems. However, in the absence of a noise-conditioning duct, aerodynamic interactions within the CROR system, as well as between the system and surrounding installation components such as the engine pylon, may result in noise penalties. If the system configuration is not optimized, the added effect of flow asymmetry to the aerodynamic interactions could potentially result in severe noise penalties, making the CROR system infeasible for use in the aircraft industry.

The proposed work will perform a sensitivity study on the design parameters of a CROR–pylon configuration. This study will leverage knowledge from past efforts with this type of configuration in order to narrow down the space of design parameters. High-fidelity computational aeroacoustics (CAA) analyses will be carried out in order to analyze the effect of each of the chosen parameters on noise. The outcome of the study is to provide a ranking, among the selected parameters in the study, that states the parameter importance for a given noise metric. This research is intended to provide both the FAA and industry with key insights necessary for the design optimization of the CROR system in the future.

The A76 project was proposed as a three-year effort with renewal on a per-year basis, and study tasks comprising the study were accordingly planned. During the first year, the aim was to determine the important parameters affecting rotor or propeller acoustics. This task then involves carrying out an extensive review in the open literature to identify previously studied and acknowledged design and operational parameters affecting rotor or propeller acoustics. The second task in the first year focused on the development of a parametric geometry model for a contra-rotating open rotor. Such a model would help to parametrically vary the open rotor geometry during computational aeroacoustics analysis needed for the sensitivity study. Tasks during the second year comprise formulating the sensitivity study as well as a limited validation effort of numerical simulations against experimental data in open rotors. The simulation campaign for the sensitivity study would comprise part of the second year and the entire third year. Such length is due to the computational cost of carrying out high-fidelity simulations for aeroacoustics.

During the development of the second year, was decided by FAA supervision that to assess confidence in numerical simulations, a more extensive validation campaign would be needed in order to assess confidence in numerical simulations. Simulations then were to be validated in a range of rotor speeds and angle of attacks in accordance flying conditions of relevance for community noise. Therefore, the research effort in the second year was re-purposed to address such validations. Finally, the A76 project was not renewed for a third year.

Task 3 - Validations of Computational Aeroacoustics

Georgia Institute of Technology

Objective(s)

This task concerns with assessing the level of agreement between numerical simulations and experiments. Therefore, this task focuses on validating predictions from high-fidelity simulations against available experimental data from an open rotor configuration in order to evaluate discrepancies between predictions from numerical simulations and experimental data.

Research Approach

Validations in this project focus on evaluating discrepancies from simulations that have been previously calibrated aerodynamically. Accordingly, the first step is concerned with calibrating simulations aerodynamically against experimental values on the F31/A31 open rotor. At low Mach conditions, loading noise is most relevant. Therefore, loading is enforced by matching the time-averaged thrust. The calibration process results in blade pitch settings that minimize discrepancies between simulated and experimental thrust. The second part concerns acoustic validation of the F31/A31 open rotor by employing calibrated pitch settings. Furthermore, validations are also carried out for nominal pitch settings.

A hybrid approach for computational aeroacoustics (CAA) is adopted. High-fidelity simulations are the focal point of the study and are thus employed. The unsteady aerodynamic flowfield is simulated by a lattice Boltzmann method (LBM) solver, whereas the far-field aeroacoustics are predicted by a Ffowcs Williams–Hawkings (FW-H) solver.

Methodology

Validation Cases and Experimental Data

The geometry of interest is the contra-rotating open rotor geometry based on a sub-scale model of the F31/A31 historical blade set, designed by GE. The front rotor geometry consists of twelve F31 blades with a tip diameter of 0.6518 m, whereas the aft rotor consists of ten A31 blades with a tip diameter of 0.6297 m [1]. NASA conducted wind tunnel experiments [1–3] on the aforementioned geometry in low- and high-speed regimes. These experiments evaluated aerodynamic and acoustic performance for approach, take-off and cruise conditions. The low-speed experiments were run in the low-speed wind tunnel (9 ft × 15 ft) at NASA facilities. These experiments targeted three pitch settings: scaled take-off (STO), nominal take-off (NTO), and approach (APP) at several rotor design speeds. Each test was run with and without a pylon. Acoustics data were gathered for a number of cases using a free-stream Mach number of $M_\infty = 0.2$, while varying rotor speed and angle of attack.

Acoustics data were collected at 18 sideline microphones, located at an offset distance of $d = 5$ ft, parallel to the axis of the model. These microphones cover geometric observer angles between 17.6° and 140°. These angles are measured with respect to the intersection of the aft blade pitch axis and the engine axis. Geometric angles lower and higher than 90° cover forward and aft locations, respectively. Specific information about microphone location has been detailed by Sree [2] and thus is not repeated here.

The present study focuses on validating cases from the low-regime experiments, specifically at the NTO pitch setting and without the pylon geometry. The experimental NTO cases [1, 2] as a function of varying operational parameters are illustrated in Figure 1, shown as black round symbols, along with the chosen cases for validation, shown as blue square symbols. The validation cases were chosen at rotor speeds spanning the upper-half range. The experimental data used in the current study came from two sources: i) NASA experiments on the F31/A31 open rotor geometry and ii) GE Aerospace data for the same F31/A31 experiments. The former source of data is employed exclusively for acoustic validations, whereas the latter is for aerodynamic calibration. These data were shared by GE Aerospace as an industrial partner in an FAA ASCENT project and are proprietary; consequently, these data are not shown.

The acoustic data employed were obtained from NASA experiments on the F31/A31 [1, 2, 4]. Three datasets were provided as supplemental information of NASA report in the form of power spectral density (PSD). The first one is the “11” set, which contains as measured spectral density; the second one is the “21” set, which comprises microphone-corrected spectra accounting for corrections due to microphone and bullet-nose sensitivity and directivity; the last one is the “41” set, containing 1-ft lossless spectra that correct for losses due to atmospheric attenuation [5].

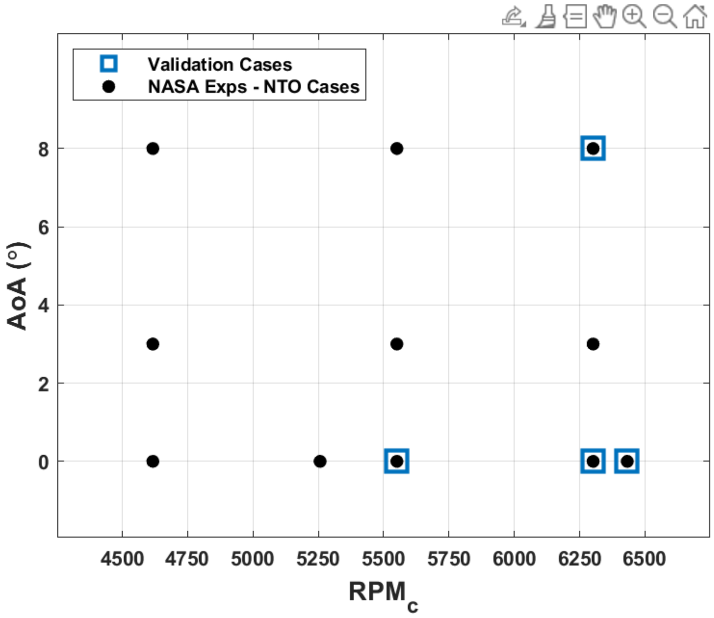

Figure 1. Validation cases. AoA: angle of attack; NTO: nominal take-off.

The current study employs the fully corrected wind tunnel measurement for validations against numerical simulations. Such fully corrected data are obtained by removing the wind tunnel background noise from the “41” data because this latter set accounts for all other corrections. The background noise is taken from the 802 RDG that contains acoustics data without blades and is applicable to all powered conditions at a zero angle of attack. [1] The details of calculating the fully corrected acoustic data is described next. First, the acoustic data are converted to a narrow-band sound pressure level (SPL) as follows:

$$SPL^* = PSD^* + 10\log_{10}(\Delta f)$$

where Δf = 12.2 Hz is the frequency bin. Next, the acoustic data for every case as well as the background wind tunnel are scaled back to their respective sideline locations. Then, the fully corrected wind tunnel measurement is obtained by removing the wind tunnel background noise according to

$$SPL = 10\log_{10}(10^{SPL^{\dagger}/10} - 10^{SPL^{\dagger}_{wt}/10})$$

Additionally, two corrections [6] are introduced. The first one ensures invalidating the above expression in cases where the background noise exceed the microphone noise level, SP L∗ wt = SP L∗ − 0.5 dB if SP L∗ wt > SP L∗−0.5 dB; while the second one corrects low frequency noise associated with the wind tunnel. Below 700 Hz noise is removed by replacing that portion of data with a parabolic function having 10 dB attenuation, relative to 700 Hz level, at 100 Hz.

Calibration in aerodynamics

Aerodynamic calibration is considered prior to acoustic validation. At the low Mach flying conditions of interest to the current study, loading noise is most relevant. [7] Since such noise type is thrust dependent, a loading equality constraint is enforced as a requirement for acoustic validation. Loading here is enforced by matching time-averaged thrust. Moreover, it is acknowledged that such time-averaged measure might not be sufficient since there may be contributions from other factors. Note, there is no attempt to directly bring CAA predictions close to experimental values, but instead evaluating CAA predictions given that a loading metric has been met.

Consider a set of calibrating parameters, collected in a vector ζ. Such parameters are generally inputs to a simulation code. Their values are unknown and thus need to be determined by a calibration process, which seeks to improve agreement between experimental data and simulation predictions. The calibration process is accomplished by minimizing a cost function:

$$\boldsymbol{\zeta}^{*} = \ arg_{\zeta} \min L$$

where the cost function, L, consists of a weighted L^2-norm measure of discrepancies between experimental aerodynamic quantities and numerical predictions:

$$L = \| \boldsymbol{w}^{t}\ \boldsymbol{\Delta} \|_2$$

Here, w is a vector of weights, expressing the importance of a particular aerodynamic quantity in the calibration process, whereas Δ is a vector containing normalized discrepancies in aerodynamic quantities between the experiments, z_i, and simulations, $\hat{z}_i$:

$$\boldsymbol{\Delta} = \begin{bmatrix} [\hat{z}(\zeta) - z_i]/z_i \\ \vdots \end{bmatrix}$$

The calibration parameters, $\zeta = [\beta_f\,, \beta_a]$, contain the pitch angles of the forward and aft rotors. respectively. Such parameters are allowed to vary around the nominal pitch setting value, $[\ \beta_f^n, \beta_a^n\ ] = [\,40.1\,°, 40.8°\,]$, corresponding to the NTO pitch setting.

The calibrated pitch angles $\zeta^* = [\beta_f^*\,, \beta_a^*]$ result from minimizing the cost function, L. This function is constructed by using experimental values of the forward and aft rotor aerodynamic performance z_i , whereas the simulation counterpart $\hat{z}(\beta_f\,, \beta_a)$ is approximated via linear regression models, fitted from training data stemming from LBM simulations. Such training data consist of forward and aft thrust from simulations for different values of pitch settings, which are varied around the nominal pitch setting. Note that the employed linear models are considered appropriate, as since departures from the nominal pitch settings are expected to be small. A total number of twelve simulations (six per calibration case, each at RPMc = 5550.5 and 6432.0) are carried out. For each case, a regression model for each rotor thrust is constructed. Simulations are carried out with discretization sizes of approximately 190 million. Note that the resulting resolution is coarser than that used for aeroacoustics predictions; however, it is considered a suitable compromise between computational cost and accuracy based on our resolution studies; which only show variation within 1% in thrust prediction between simulations at different resolutions.

Validation in acoustics

Acoustic validations are carried out using the pitch blade settings resulting from the aerodynamic calibration. Additionally, a validation case at the nominal pitch setting (NTO) is also included in order to contrast numerical prediction against the calibrated case. Such a case is chosen at the lowest rotor speed among the considered cases as shown in Figure 1. Furthermore, this case will also serve as a reference to bring forth the effects of calibration on the acoustical results.

The rotor speed range in the present acoustic validations focus on the upper-half of the rotor speed span in the F31/A31 experiments. International Civil Aviation Organization (ICAO) certification limits the effective perceived noise level (EPNL), a human-hearing-weighted and time-averaged metric of overall sound level, of every aircraft it certifies. This process examines three flight conditions, i.e., take-off, flyover, and approach, and compares the resulting EPNL versus a maximum value. Since the takeoff and flyover flight regimes are dominated by engine noise, as opposed to approach and airframe noise, these flight rotor speeds will continue to be the focus of this study. The calibration and validation cases addressed in the current study are a subset of the NASA experiments [1, 2] at the NTO pitch setting, as shown in Figure 1.

The frequency range is one important aspect to consider in this study. The ideal frequency range to be addressed in the current study should cover the entire the high annoyance portion - human hearing constraint - of 10 kHz. Such value applies to the full scale model, whereas in the wind tunnel model said threshold increases to 50 kHz due to the scale factor of 5 respect to the full scale model. [1] Simulations in the current study attempt to address a part of the high annoyance portion. Consequently, most overall noise metrics will be computed in the range of 0.5–50 kHz for consistency with experiments.

The metric for validation between experiments and simulations adopted in the current study is the overall sound pressure level (OASPL). It has been pointed out [8] that in the resulting acoustics data the F31/A31 open rotor experiments, the acoustic energy is distributed among all shaft order tones, opposed to the specific orders as predicted by theory. As a consequence, it has been argued that OASPL should be a good metric in spite of the distribution of acoustic energy among tones [8].

Computational Analysis and Set-up

Simulations in the current study rely on a hybrid strategy for computational aeroacoustics (CAA) analysis. The unsteady aerodynamics flowfield is simulated by means of a lattice-Boltzmann method (LBM) solver. During the runtime of the aerodynamic solver, flowfield data are collected at specified surfaces. Such data are then used as an input to a far-field acoustics solver. An acoustic solver, based on the FW-H equations, is then employed for predicting far-field acoustics. Both the aerodynamics and acoustics methods are described in more detail below.

Geometry employed on simulations

The geometry employed in the current study is the contra-rotating open fan based on the GE designed F31/A31 blades. The geometry includes the nacelle as well as the rotating hub for both front and aft rotors. Nevertheless, the simulated geometry does not include the blade to blade angle variation from the assembly process that is present in the experiment [8] since such information is not available. The simulated geometry uses a purely cylindrical aft nacelle extension as opposed to the test article which was installed using a nacelle extension with a varying sectional radius. Moreover, the geometry used in the current simulations does not include gaps in junctions, such as those found between the nacelle and rotating hubs and between the blades and hubs.

The F31/A31 shape employed in the current study is that of the max climb flight condition. The geometry was provided with blade pitch settings of 60.5°/59.0°. Any blade pitch setting addressed in the current study is thus set from the aforementioned forward and aft pitch angles. Moreover, it is important to point out the blade shapes are fixed to the aforementioned flight condition regardless of the operational parameters utilized in the simulated cases. The aeroelastic deformation has implications in aerodynamics and acoustics performance. The balance between aerodynamic, centrifugal and Coriolis forces results in blade deformation, especially in the outward-half span of the blades. As previously investigated, [9] blade deformations due to the operating point influence both aerodynamic and acoustic performance. Larger deformations are observed at the cruise condition, followed by the take-off condition and approach. Differences in shapes between unrunning and running blades exhibited differences of around 5% in thrust coefficient predictions. Thus, the study found that accounting for blade deformations improves simulation predictions. Ideally, every operating condition in simulations should use the corresponding deflected shape. Unfortunately, lack of information on blade shapes prevented accounting for such effects. Therefore, the only available shape - at max climb - is employed in all cases examined in the current study.

Unsteady Aerodynamics

The unsteady aerodynamic flowfield is obtained by employing a commercial lattice-Boltzmann method (LBM) solver, PowerFLOW. Whereas traditional fluid solvers, which are - based on the continuous assumption via Navier-Stokes equations - solve for macroscopic quantities; LBM solves for the Boltzmann equations by tracking the evolution of microscopic particle distributions in the fluid and thus modeling occurs at a mesoscopic scale - simplified microscopic behavior - where the physics are more fundamental. Consequently, the conserved fluid quantities are not directly modeled, but instead obtained indirectly by integrating locally over the particle distribution functions. The compressible Navier-Stokes equations of fluid dynamics are recovered through the Chapman-Enskog expansion. Such modeling results in low dispersion and dissipation properties, which in turn makes it very desirable for aeroacoustic purposes.

Origins of LBM can be traced back to the lattice gas automata (LGA) method. In this method, fluid flow is simulated by tracing motion through advection and collision of fluid particles on a regular lattice by employing the Boolean fluid model. However, in LBM, continuous particle distributions are employed, similar to particle distribution functions in kinetic theory. This adoption improves upon the shortcomings of LGA, such as noise and limitations in transport coefficients. LBM primarily encompasses two steps, collision and propagation. The collision step occurs when particles with different velocities arrive and interact at the same node. While the propagation step involves particles traveling to their nearest neighbors in the direction of their prescribed velocity after collision. The LBM scheme for fluid dynamics consists of the time evolution of the distribution function, which is governed as follows:

$$\boldsymbol{f_i(x + \xi_i \Delta t, t + \Delta t) = f_i(x, t) + \Omega, \quad i = 1 \dots n}$$

where f_i and $\boldsymbol{\xi}_i$ are the particle distribution function and the particle speed in direction i, respectively, while Δt is the time step. The term on the right hand side expresses the collision operator term which is modeled by the Bhatnagar-Gross-Krook (BGK) single relaxation time model:

$$\Omega = -\frac{f_i(\boldsymbol{x}, t) - f_i^{eq}(\boldsymbol{x}, t)}{\tau}$$

Where f_i^{eq} is the equilibrium distribution function and τ is the relaxation time parameter. This model assumes a constant rate relaxation to equilibrium for the particle distribution function. The governing equations is explicitly advanced in time in a lattice with prescribed n particle velocity directions. The macroscopic quantities of the fluid are simply obtained by integrating the distribution functions over the velocity space; for instance, density and momentum are given by the following expressions:

$$\rho(\boldsymbol{x}, t) = \sum_i f_i(\boldsymbol{x}, t)$$

$$\rho \boldsymbol{u}(\boldsymbol{x}, t) = \sum_i \boldsymbol{\xi}_i f_i(\boldsymbol{x}, t), \quad i = 1 \dots n$$

Turbulence modeling is achieved by means of very large eddy simulation (VLES). Moreover, in order to reduce the spatial resolution requirement in near wall regions, a hybrid wall-treatment model is chosen. This modeling is based on the standard log law of the wall and includes a laminar sub-layer model to account for the effects of favorable and adverse pressure gradients.

Boundary conditions are defined as follows: in the outer boundaries, pressure/velocity boundary conditions are prescribed, whereas non-slip wall boundary conditions are prescribed on surfaces of both rotors and nacelle. In the nacelle extension, however, slip wall boundary conditions are prescribed in order to avoid influences of boundary layers in those locations. Boundary values (V_∞, T_∞, p_∞) as well as rotor speed in the current simulations are set to those of the wind tunnel conditions and actual rotor speed as measured in the F31/A31 experiments; however, their values are not shown due to proprietary restrictions.

The computational domain is decomposed into: (i) inner cylindrical regions for the forward and aft rotors, respectively, each with its own rotating reference frame using a sliding mesh approach to model forward and aft fan rotation; and (ii) an outer cubic region with a stationary reference frame. The LBM scheme is explicitly advanced in time in a Cartesian volume mesh around the geometry under study. Spatial discretization is achieved via variable refinement (VR) regions. Such regions are comprised of specified volumes within the computational domain. A level defining the spatial resolution is assigned to each region. The spatial resolution increases two-fold with VR level. Several VR regions in locations of interest are defined within the computational domain. VR regions consisting of small cylindrical volumes are defined by tracing the blades' leading and trailing edges as well as blade tips. VR regions around blade surfaces are defined by three different offset volumes. Moreover, VR regions are also defined for tip vortexes as well as blade wakes. Another VR region is defined by the volume encompassing fifty percent of the outer span of the forward rotor. At the inter-rotor space a VR region is also defined. Each rotating region also defines a VR region as well. Finally, other VR regions are created in order to progressively decrease resolution away from the open fan configuration. Each of the aforementioned regions is assigned a VR level as shown in Table 1. The highest resolution is 0.125 mm and in turn defines the solver time step of 1.7×10^{-7} secs, approximately. The typical discretization size for simulations in the current study is approximately 900 million voxels. Such size is the upper limit that can computationally be afforded in the current study.

Simulations are initialized with a uniform velocity corresponding to the free-stream value on coarse meshes of approximately 190 million voxels, and advance in time for 6 revolutions so that the near flowfield is unaffected by the initial condition. The resulting flowfield is then employed to run the full simulation. Unsteady flow data for aeroacoustic analysis is collected once the flow is established. The flow is considered established after 6 rotor revolutions when the flow has adjusted to the finer discretization. Computation of the full simulation requires approximately 110,000 single CPU hours on a 2.7 GHz Intel Xeon Gold 6226 processor cluster.

Table 1. Variable Refinement (VR) regions description.

VR	Detail
15	LE & TE blade edges, and blade tips
14	Tip vortexes and blade inner
13	Blade wakes, Blade mid and Outer blade span
12	Inter-rotor and Blade outer
11	Forward and aft rotating region
⋮	
0	Outer boundaries

Far-Field Aeroacoustics

Far-field aeroacoustics is predicted by means of a commercial Ffwocs Williams - Hawkings (FW-H) solver, PowerAcoustics. Moreover, in order to prevent acoustic reflections from outer boundaries, a sponge region surrounding the open rotor geometry towards the outer boundaries is considered. In said region, the fluid kinematic viscosity is progressively increased so that out-going acoustic waves are dissipated.

The FW-H solver processes transient flow data recorded at specified surfaces during the simulation of unsteady aerodynamics in order to propagate acoustics to the far-field. The upper frequency value intended to be modeled in the acoustic study influences the choice of the type of FW-H surface. Surfaces of the permeable type would be defined surrounding the open fan configuration, while impermeable type would be defined at the rotor surfaces. Permeable surfaces allow capturing noise sources with scattering or reflection effects at the expense of high spatial resolution inside the volume encompassing the FW-H surface. Impermeable surfaces, on the other hand, do not impose such a resolution requirement at the expense of not capturing scattering or reflection effects. Employing permeable FW-H surfaces for addressing, even partially, the high annoyance portion of noise spectra would impose such a high spatial resolution that would make simulations intractable for the current study. The choice is then to employ impermeable FW-H surfaces. These surfaces are defined at both rotor surfaces, not only including blades but also the hub rotating part.

Acoustical data are obtained at two sets of sideline receivers. The first one is the sideline receivers as described by experiments, [2] which are located at a distance, d = 5 ft. This set consists of 18 receivers, spanning from approximately 17.5° to 140°, and it is uniquely used for calculating discrepancy measures for comparison with experimental results. Likewise, the second set also consists of sideline receivers located at the same distance d, but with a higher spatial resolution of 2.5° separation, and spanning a larger range of angles, 15° to 160°. The arrangement of acoustic receivers is illustrated in Figure 2.

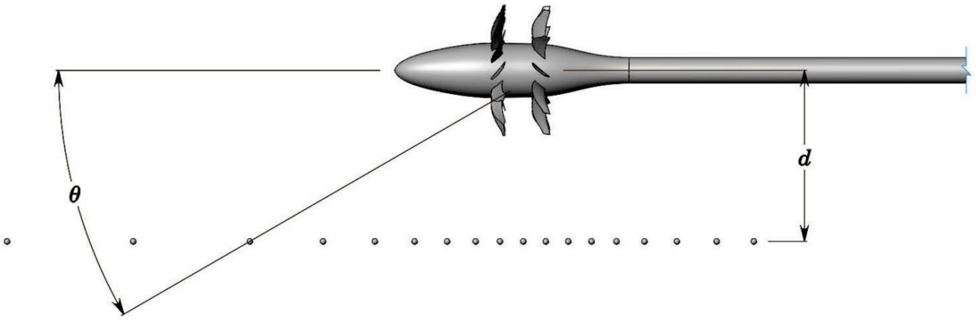

Figure 2. Arrangement of receivers at zero AoA.

Note: Geometry is a generic contrarotating open rotor and thus it is not the GE F31A31

* A generic open fan geometry is used for the illustration since F31/A31 geometry is GE proprietary

For the non-zero AoA cases, the distances to the microphones on the sideline array changes respect to the distances of that at zero AoA, in accordance to descriptions in NASA reports [1, 4], as shown in Figure 3. In order to incline the open fan model to a certain AoA different from zero, the model is rotated around a turn table, which pivot point is located 33.162 inch downstream of the reference point – aft pitch axis, while the microphones remain fixed. Consequently, at a non-zero AoA distances to microphones differs from those at zero AoA. Indeed, microphones in forward and aft direction are farther and closer, respectively, than in the AoA = 0 case. Moreover, directivity angles are also different than in the AoA = 0 case. Because of the above, acoustic validations for non-zero AoA cases are reported as a function of microphone label number rather than directivity angle, θ. Moreover, any calculation, e.g. attenuation correction, power level and so on, is carried out accounting for actual distances according to the non-zero AoA arrangement.

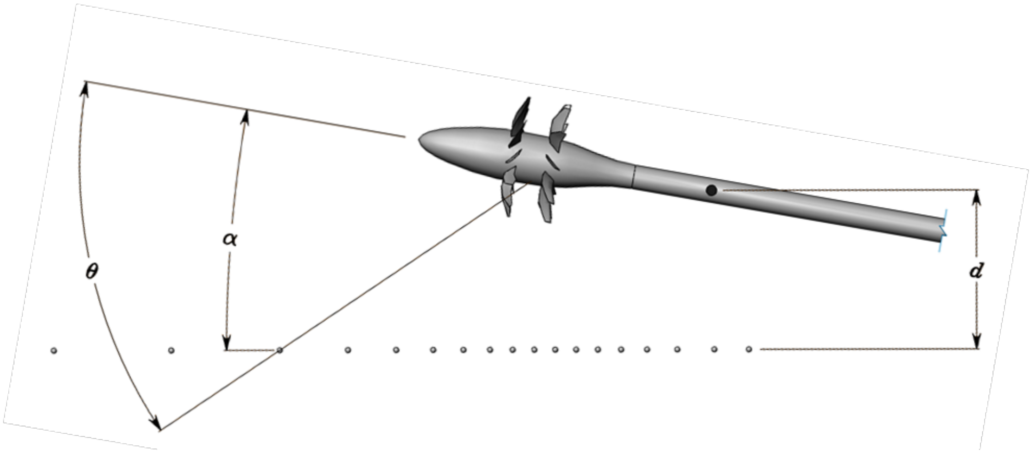

Figure 3. Receiver arrangement at non-zero AoA.

Note: Geometry is a generic contrarotating open rotor and thus it is not the GE F31A31

Flow data is recorded at the aforementioned impermeable FW-H surfaces for collection time periods between 12 - 16 rotor revolutions and at a rate of approximately 190 kHz. Spectral data is obtained by applying the Fourier transformation to the resulting data from the acoustic solver. The employed window width is 50% and a parabolic Welch windowing function with 50% overlapping is applied to the time-pressure data resulting from the acoustic solver.

Aeroacoustics results are examined by overall noise metrics such as overall sound pressure level (OASPL) and overall power level (OWPL). One-third octave spectra as well as source power level (PWL) spectra are also examined. OPWL is calculated by integrating the PWL spectrum along the frequency domain. PWL [10, 11] is obtained from the following expression:

$$PWL(f) = \frac{1}{\rho_\infty c_\infty}\int_0^{2\pi}\int_0^{\pi}[1 + M_\infty \cos(\theta_e)]^2\, p^2(f,\theta_e,\psi) r_s^2 \sin(\theta_e)\, d\theta_e d\psi$$

and expresses the acoustic energy per frequency independent of direction by integrating acoustic pressure on a spherical surface around the open fan under study. In the above expression, p^2 is obtained from the sound pressure level (SPL) broadband spectra, r_s is the radius of a spherical surface surrounding the open fan under study, M_∞, ρ_∞ and c_∞ are the free-stream Mach number, density and speed of sound, respectively. Moreover, f is the frequency, $\theta_e = \theta - \sin^{-1}(M_\infty \sin\theta)$ is the emission angle, while ψ is the azimuthal angle - revolving around the propulsor axis. The above expression is converted into spectrum, in dB, by previously using a reference sound power, $PWL_0 = 10^{-12}$ W.

Results: Validations for calibrated pitch cases

Calibration in Aerodynamics

The cost functions of thrust (L_T) and torque (L_Q) as a function of both forward (β_f) and aft (β_a) pitch angles are shown in Figure 4. Depending on the aerodynamic performance quantity chosen for the cost function, the calibration process leads to different sets of pitch angles - minimum location of the respective cost function as noted by the isocontour curve levels. As a consequence, optimal pitch angles that simultaneously minimize thrust and torque discrepancies are not attainable. Such feature is also found at other rotor speeds, although not reported for the sake of brevity.

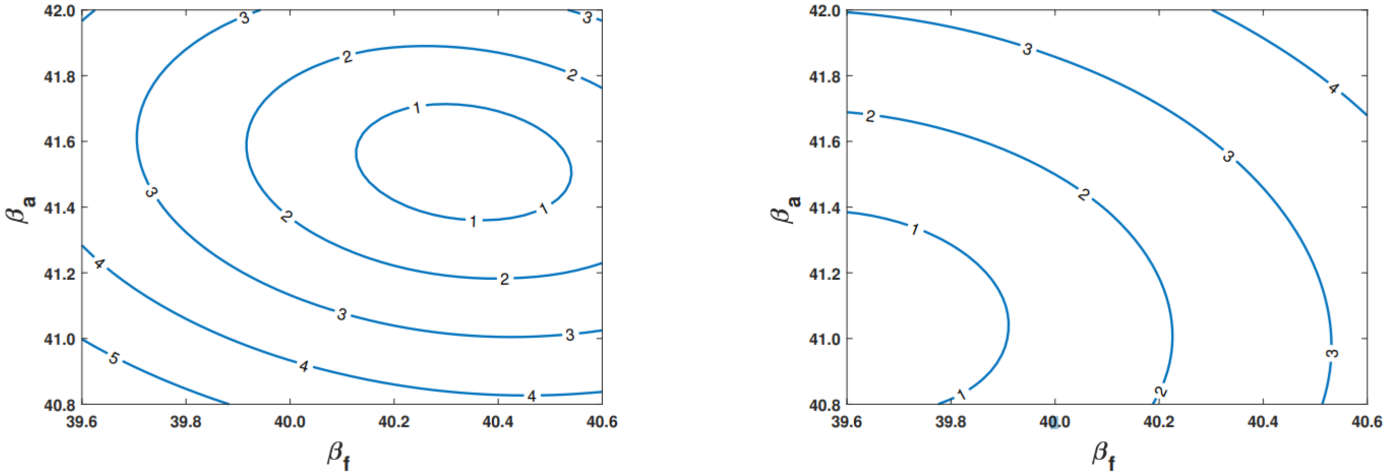

(a) L_T: Thrust-based cost function (normalized)

(b) L_Q: Torque-based cost function (normalized)

Figure 4. Thrust and torque cost functions, RPM_c = 5550.5.

The outcome of minimizing these cost functions based are shown in Table 2. Angular departures (δβ) from the nominal pitch setting, such that: $\beta^* = \beta^n + \delta\beta^*$, are reported. As illustrated in the above figure, calibrated pitch settings are different. Thus, calibration based on a combined cost function, involving both thrust and torque, would not minimize either one but would be a compromise between them.

Table 2. Calibration based on L_T and L_Q at RPM_c = 5,550.5.

Cost Function	$\delta\boldsymbol{\beta}_f^*$	$\delta\boldsymbol{\beta}_a^*$
Thrust, L_T	+ 0.288°	+ 0.709°
Torque, L_Q	- 0.500°	+ 0.274°

As stated in Section II, thrust matching is chosen as the criterion for calibration. The reason behind this is the dependence of loading noise on thrust. Moreover, it is found that depending on the rotor speed of interest, enforcing thrust leads to different calibrated pitch settings, Therefore, calibration hereafter proceeds individually for every validation case. Results from aerodynamics calibration are shown in Table 3. Note that at all rotor speeds investigated in this study, the resulting pitch angles slightly increase over the nominal one due to thrust underprediction at the nominal angles. Moreover, after calibrating, thrust is re-calculated from higher-resolution LBM simulations - as needed by aeroacoustics. Hence, the resulting thrust my vary slightly; however, discrepancy by individual rotor is within 1 %, which is in accordance with experimental uncertainty. [1] Also, calibrated pitch at RPM_c = 6250.5 is taken as the one at the highest rotor speed since predicted thrust is found within the acceptable threshold for calibration.

Table 3. Resulting calibrated pitch setting.

RPMc	**Cost Function**	$\delta \beta_f^*$	$\delta \beta_a^*$	***Remark***
5550.5	Thrust, L_T	+ 0.288°	+ 0.709°	
6250.5	Thrust, L_T	+ 0.460°	+ 0.428°	same as highest rotor speed
6432.0	Thrust, L_T	+ 0.460°	+ 0.428°	

Comparisons of net thrust resulting LBM predictions and previous simulations [12] against experimental measurements are shown in Figure 5. All solvers predict thrust trends with rotor speed as seen in Figure 5(a); however, at the nominal pitch setting all solvers exhibit some degree of discrepancy from experimental measurements as shown in Figure 5(b). In contrast, LBM simulations at calibrated pitch setting exhibit the smallest discrepancy due to the thrust matching process. Furthermore, there are apparent variations in predictions among solvers at nominal pitch settings. Corresponding LBM simulations underpredict thrust at all rotor speeds, whereas the other two solvers generally overpredict. Levels of discrepancy are smaller for the OVERFLOW solver, whereas the FUN3D solver and LBM simulations exhibit comparable magnitudes of discrepancy.

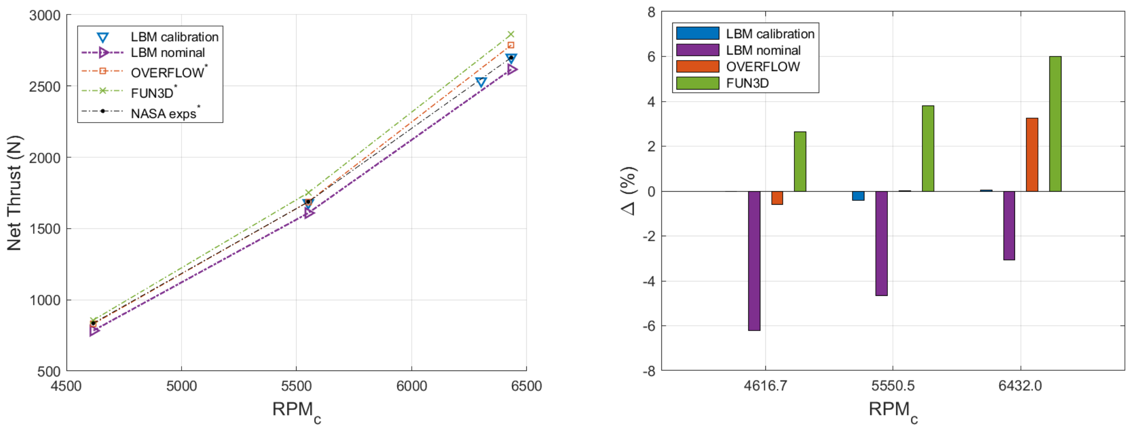

Figure 5. Thrust comparisons: Thrust (left) and discrepancy (right).

Torque ratio predictions from LBM simulations and previous studies [12] against NASA experiments are shown in Figure 6. At the nominal pitch setting, none of the solvers capture trends accurately as seen in the left plot. Indeed, all solvers predict monotonically decreasing trends with rotor speed, while NASA experiments exhibit a nearly flat trend. LBM simulations with calibrated pitch settings, on the other hand, result in a qualitatively closer trend. All simulations with the nominal pitch setting exhibit significant departure from experiments at the lowest rotor speed; however, departures decrease with rotor speed as shown in the right plot. Also, note that the effect of calibrating is not much different at the highest rotor speed compared to the nominal pitch setting. Finally, another numerical study [8] with the nonlinear harmonic (NLH) model reported thrust and torque ratio discrepancies of 1.6% and 9.0%, respectively, on average for six cases with corrected rotor speed ranging between 4620 - 6436 RPM_c.

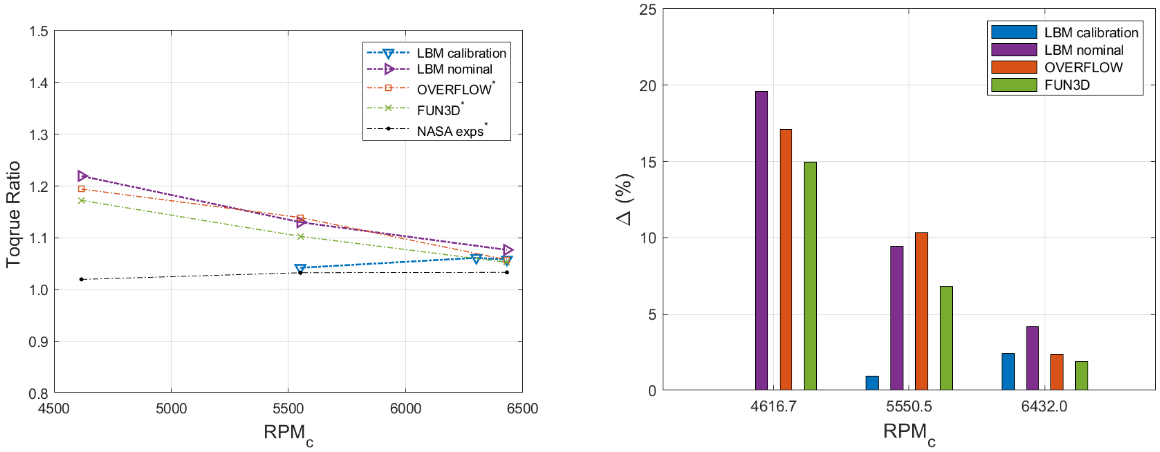

Figure 6. Torque ratio comparisons*: Torque ratio (left) and discrepancy (right).

*Values digitized from Nark et al. [12]

<u>Validation in Acoustics</u>

In this section, the findings on predicted noise obtained from propagation to the far-field, by integrating the FW-H equations on impermeable surfaces are presented. Numerical predictions are contrasted against NASA experimental measurements from complimentary data to the NASA report. [1] Quantification of agreement between experiments and numerical predictions are accomplished by computing metrics of discrepancy. These are simply differences between experimental and numerical values, or averaged discrepancy - root mean squared differences. For consistency with experiments, discrepancies are solely calculated from signals computed at the same locations of the acoustics probes in the F31/A31 experiments, [1, 2] whereas trends from numerical predictions are shown at a higher angular resolution. Acoustic quantities for comparisons comprehend overall sound pressure level (OASPL) as well as overall power level (OPWL). These are calculated within a frequency range of 0.5 to 50 kHz for consistency with experiments.

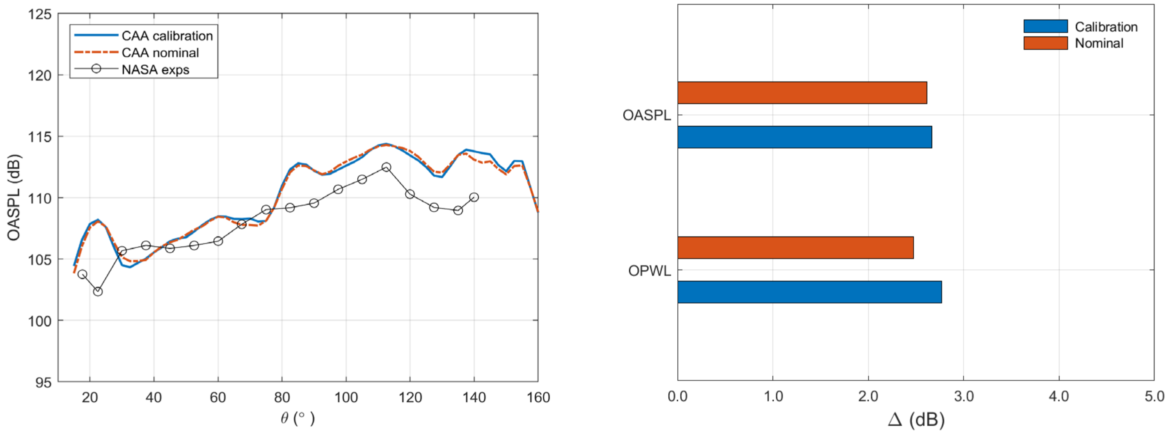

(a) OASPL directivity (b) OASPL and OPWL average discrepancy

Figure 7. Comparison between nominal and calibrated pitch settings.

Validations contrasting the effect of calibrating to the nominal pitch setting are shown in Figure 7. Directivities of OASPL as predicted by simulations along with that of experiments [1] are shown in Figure 7(a), while respective average discrepancies are shown in Figure 7(b). Predictions are from medium resolution simulations of about 600 million voxels. There is noticeable variation in agreement between simulations and experiments along directivity angles. Small differences are found for intermediate angles - between 25° and 80° - whereas differences increase for smaller and larger forward and aft angles, respectively. Moreover, note that no noticeable differences in OASPL directivity are found between predictions at the nominal and calibrated pitch settings. Average discrepancies of OASPL and OPWL are shown in Figure 7(b). When comparing between calibrated and nominal pitch settings, small changes in discrepancy are found between calibrated and nominal pitch setting, 0.05 dB for OASPL and 0.29 dB for OPWL. Such relatively small increments in discrepancies on the calibrated pitch setting is attributed to the increase in thrust in the calibrated case relative to the nominal case. Such increase is also consistent with the increasing behavior of sound power level with thrust previously reported in experiments. [1]

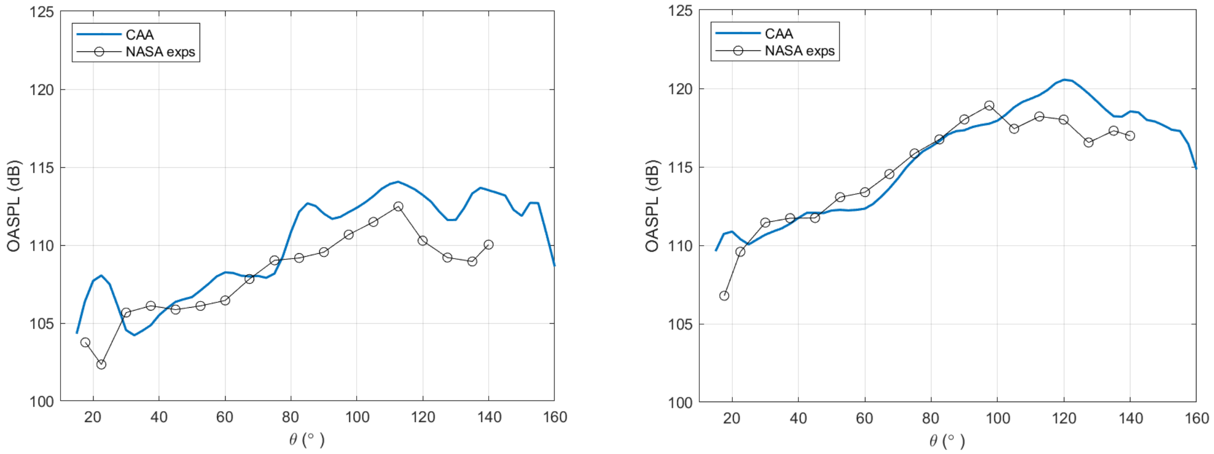

(a) RPM_c = 5,550.5 (b) RPM_c = 6,301.4

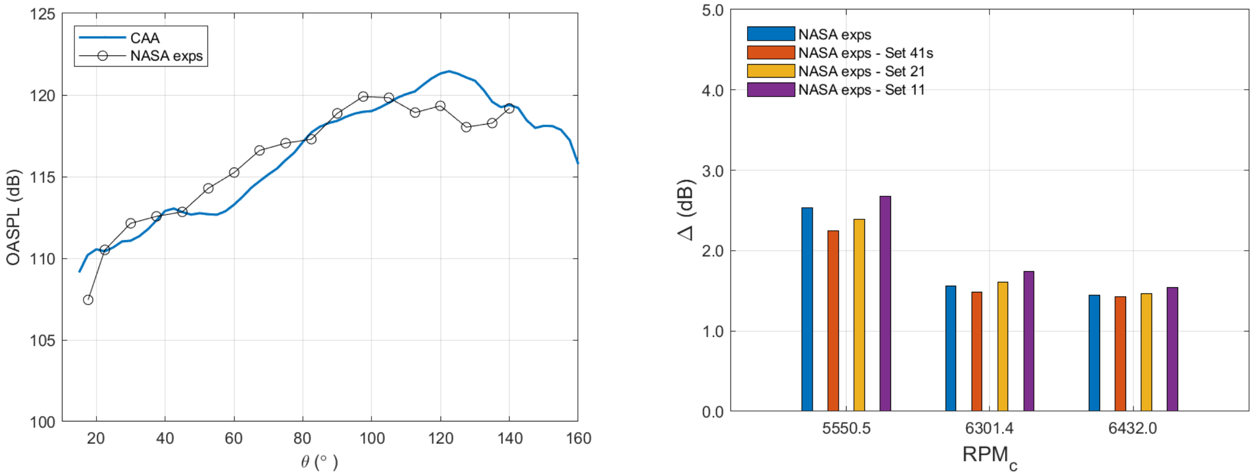

(c) RPM_c = 6,432.0 (d) OASPL discrepancy

Figure 8. OASPL sideline directivity and respective discrepancies with experiments.

OASPL directivity with rotor speed as well as their corresponding averaged discrepancies for all calibrated cases are shown in Figure 8. Small changes in OASPL values are observed at any directivity angle for the two highest rotor speeds due to their proximity in RPMc value. Moreover, closer agreement in trend and values are seen at the two highest rotor speed, shown in Figure 9(b) and (c), specifically for directivity angles between 20° and 100°. The corresponding discrepancies at every rotor speed are shown in Figure 8(d). In order to illustrate the effect of different corrections in the experiment measurements, discrepancies are calculated with respect to all relevant sets of the experimental data as previously described. Note that

partial correction in experimental data could lead to variations of discrepancy between 0.2 to 0.5 dB. Nevertheless, the actual discrepancy is measured with respect to the fully corrected data shown in the blue bar. Values around 1.6 dB are found for the two highest rotor speeds, whereas the discrepancy is larger, 2.5 dB approximately, for
the lowest rotor speed.

Spectral representation of the far-field sideline noise directivity for the highest rotor speed is shown in Figure 9. A map of one-third octave spectra are plotted between 0.5 to 30 kHz. Although not perfect, some discernible similarities - qualitative and quantitative - could be found between the spectra from simulations, Figure 9(a), and that of experiments, Figure 9(b). Simulations reasonably predict the regions of large SPL values, located above 2.5 kHz and for directivity angles larger than 60°, although there is some overpredictions at higher frequencies - above 15 kHz - between sideline angles of 80° and 120°, approximately. Furthermore, simulations also predict the smaller regions containing the highest sound pressure level with a consistent frequency range - between 3.0 and 8.0 kHz approximately - although numerical predictions are shifted to the aft direction. Finally, simulations exhibit a very small region with peak values not observed in the experiments, around 120° and 3.2 kHz.

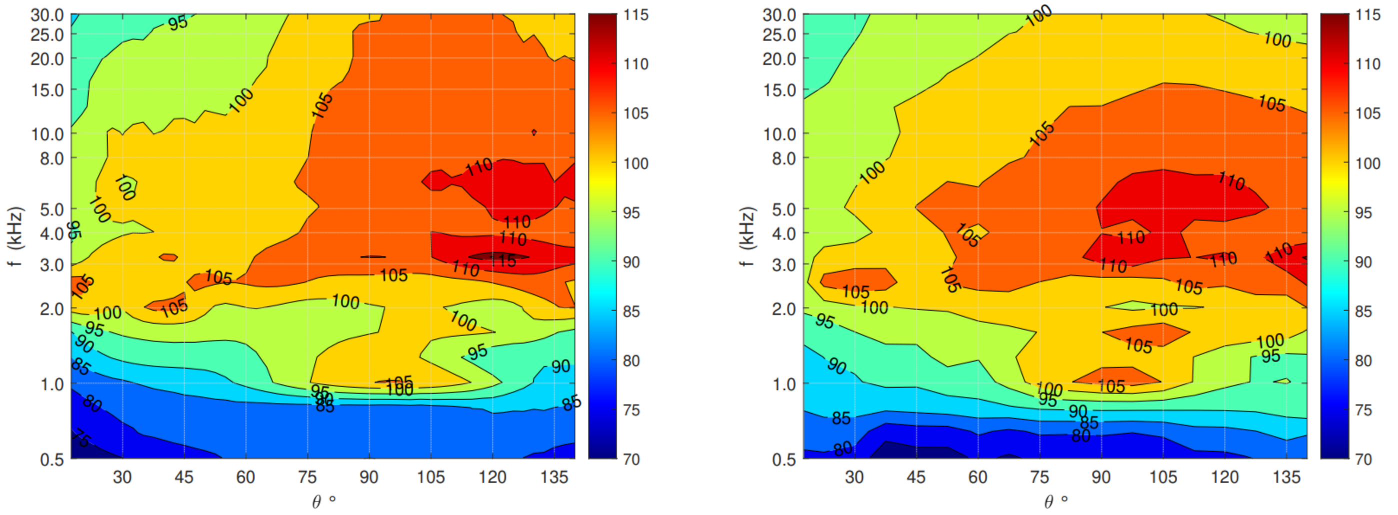

(a) Simulations

(b) NASA Experiments

Figure 9. Sideline directivity in one-third octave SPL spectra (dB) at RPMc = 6432.0.

One-third octave spectra for the two highest rotor speeds at three different receivers are shown in Figure 10. These receivers are located at a forward position, θ = 45°, plane of the aft rotor θ = 90°, and an aft location, θ = 135°. Levels of discrepancy between simulations and experiments seem comparable for the two rotor speeds at every receiver. Moreover, at the forward receiver, shown in Figure 10(a) and (b), even though there are similarities in trend, the acoustic energy is more prominent within bands between 2 - 4 kHz in the simulation, whereas the in the experiment this occurs between 4 - 6 kHz. At the plane of the aft rotor and the aft receiver, shown in Figure 10(c) - (f), there is agreement in the location of frequencies with the most acoustic energy; however, there is some overprediction toward the higher frequencies at these receivers, more noticeable beyond 15 kHz as noted previously in Figure 9. At higher frequencies, there is more agreement at the forward receiver, which can also be observed in the spectral map in Figure 9.

Source power level spectra comparison between experiments and simulations for the highest rotor speed is shown in Figure 11. The tonal content is quite apparent in the spectra, while the broadband content is noticeable. Distinctive tonal content can be observed up to 16 kHz although a great portion of the tonal content is more concentrated up to 12 kHz, which is in accordance with experiments. [4] In the simulation, the PWL spectrum reveals that the highest source power levels are observed at frequencies that are even multiples of the shaft frequency. The PWL spectrum calculated from experimental data not only exhibits high levels at even shaft orders but also odd ones. Such difference in the numerical predictions suggests that the acoustic energy is distributed somehow differently in the simulations. Based on theory grounds, it has been argued [8] that such behavior results from difference in geometry between simulations and in wind tunnel, primarily variations in the installed pitch from blade to blade.

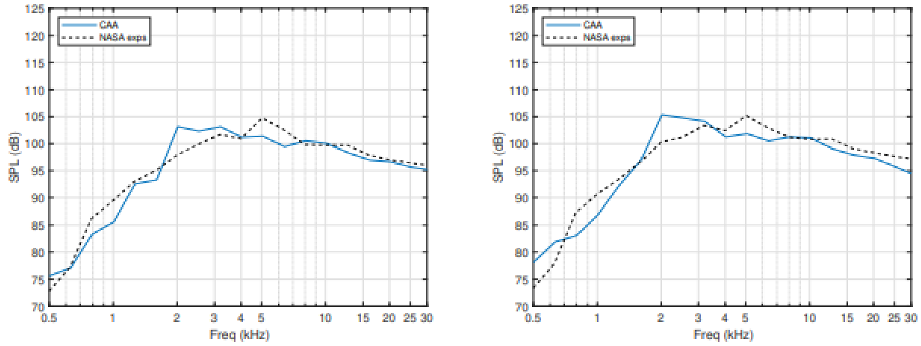

(a) Spectrum at $\theta = 45^\circ$ (b) Spectrum at $\theta = 45^\circ$

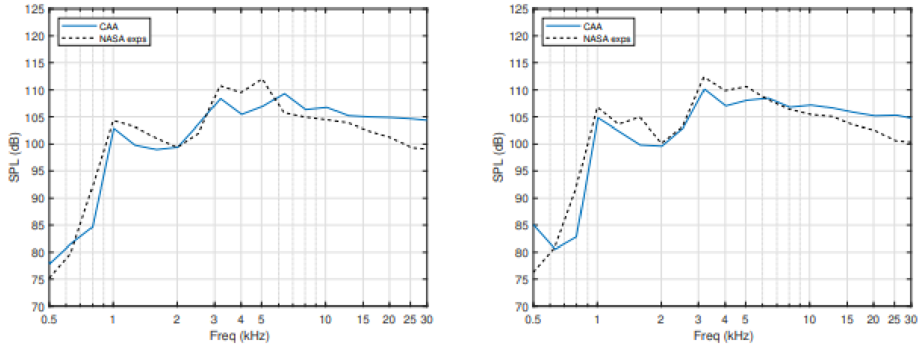

(c) Spectrum at $\theta = 90^\circ$ (d) Spectrum at $\theta = 90^\circ$

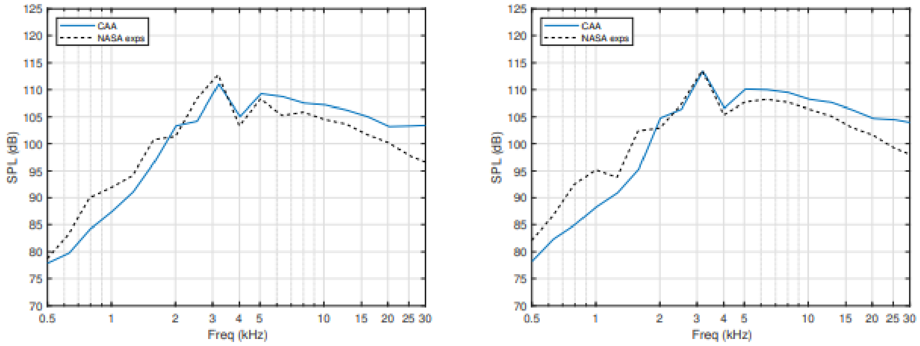

(e) Spectrum at $\theta = 135^\circ$ (f) Spectrum at $\theta = 135^\circ$

Figure 10. One-third octave spectra, RPMc = 6301.4 (left) and RPMc = 6432.0 (right).

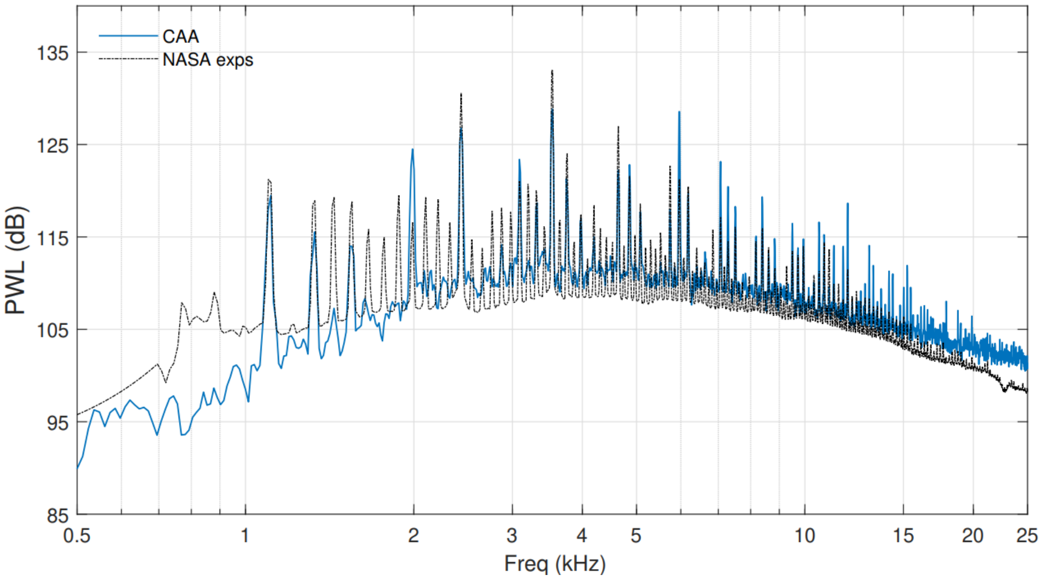

Figure 11. Source power level spectrum, RPMc = 6432.0.

Acoustic energy generated by the open fan configuration is calculated by means of overall power level (OPWL). This quantity is calculated by integrating the source power level spectrum (PWL) for frequencies between 0.5 to 50 kHz. The PWL spectrum is obtained by assuming axisymmetry with respect to propulsor axis, ψ ∈ [0, 2π], and is calculated by only using the same receiver locations used in experiments for consistency. The sideline acoustics data is mapped into a constant radius, equal to the sideline distance d, by assuming spherical spreading. [1] Comparisons of OPWL calculated from simulations and that of experiments are shown in Figure 12. The OPWL trends with corrected rotor speed are in qualitative agreement with experimental trends. Closer agreement is found above 6000 RPM$_c$ although it reduces at lower speeds. Numerical predictions are closer to the experimental values at the two highest rotor speeds, with an average discrepancy of less than 1 dB, whereas larger values of 2.8 dB are found at the lowest rotor speed as shown in Figure 12(b).

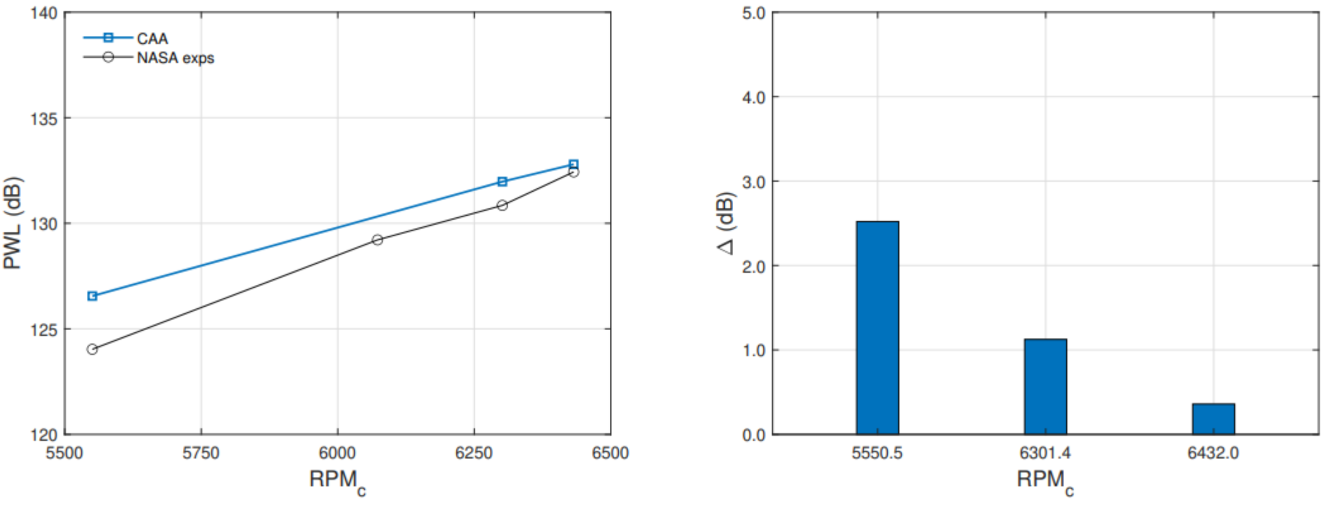

(a) Overall PWL trends

(b) Overall PWL discrepancy

Figure 12. Overall PWL.

The case at a non-zero AoA is chosen at the second highest rotor speed and angle of attack among the F31/A31 experimental cases. The operational parameters are then RPMc = 6304 and AoA = 8. Comparison of overall sound pressure level (OASPL) from numerical predictions and experiments are shown in Figure 13, left plot. In addition to the impermeable FW-H approach, predictions using a permeable FW-H are also shown. Due to spatial resolution the permeable approach is limited to 12.5 kHz. Note that OASPL is plotted as a function of microphone label with number increasing from the forward to the aft locations. The impermeable approach in average provides close predictions in all microphones. In contrast, the permeable approach prediction are closer at intermediate microphones but prediction rapidly worsens for microphones in the aft region due to the length of the FW-H surface that is not able to cover farther aft locations. OASPL discrepancy trend with angle of attack is also shown in Figure 13, right plot. An increment of approximately 0.20 dB is observed as consequence of the increment in AoA.

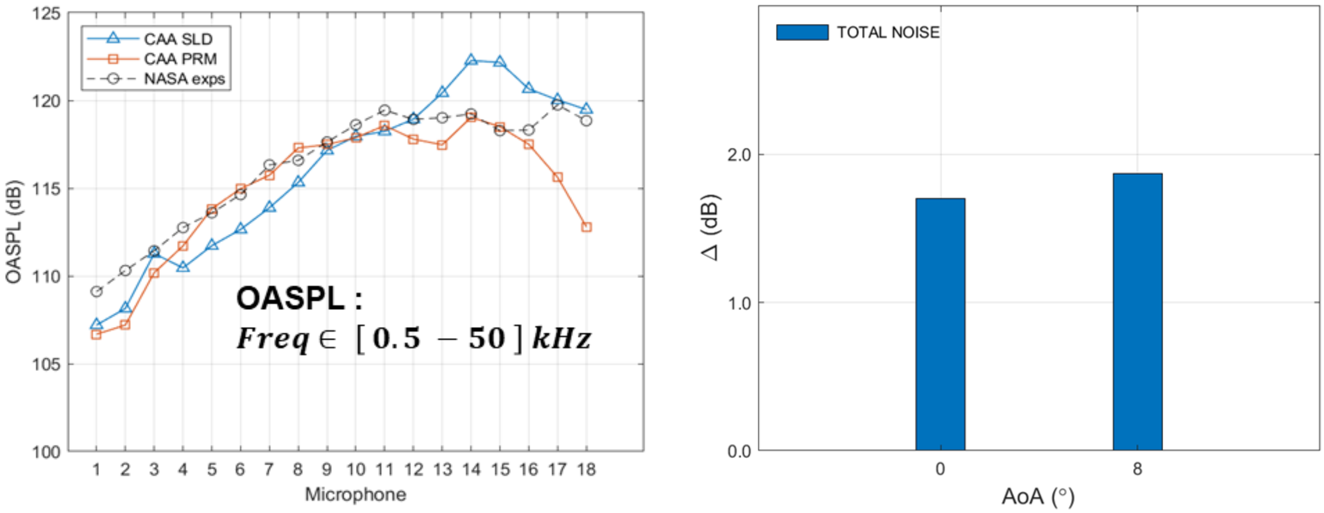

Figure 13. OASPL validation at AoA = **8**° (left) and discrepancy trend with AoA (right).

Results: Validations for nominal pitch cases

At the nominal pitch settings, two cases are carried out to evaluate the acoustics as a function of angle of attack (AoA) at a nearly fixed corrected rotor speed of RPMc = 6304. Simulations are carried out as previously described for the calibrated cases with the exception that acoustics are additionally predicted by a FW-H formulation that considers the convective effects of the free-stream. The commercial acoustic solver OPTYDB, a recent addition to the PowerFLOW suite, recently made available to research in the FAA A76 project, is employed for such an end. It is pointed out that results with the latter approach are considered the standard for comparison. This is because it possesses all the features needed to simulate far-field acoustics, such being able to predict the frequency range of interest as well as considering the effect of the free-stream. Such features were lacking on the permeable and impermeable approach previously used.

OASPL directivity in terms of directivity angle and microphone label are presented in Figure 14 for the AoA = 0° and AoA = 8° cases, respectively. OASPL is calculated in the 0.5 – 50 kHz frequency range. The OASPL discrepancy for this case is not larger than 1.3 dB with the non-zero AoA exhibit slightly smaller discrepancy as seen in Figure 15.

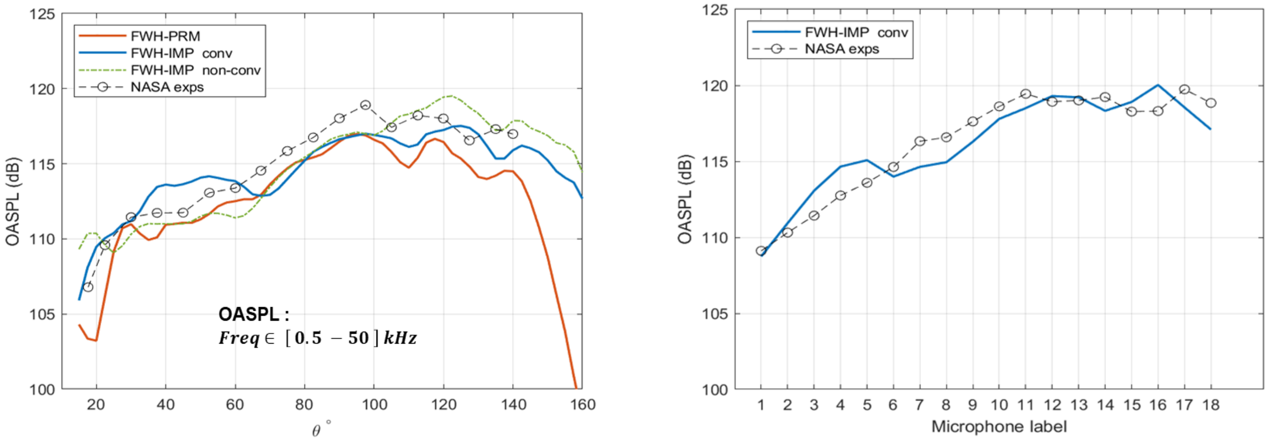

Figure 14. Total noise OASPL: AoA = **0**° (left) and AoA = **8**° (right).

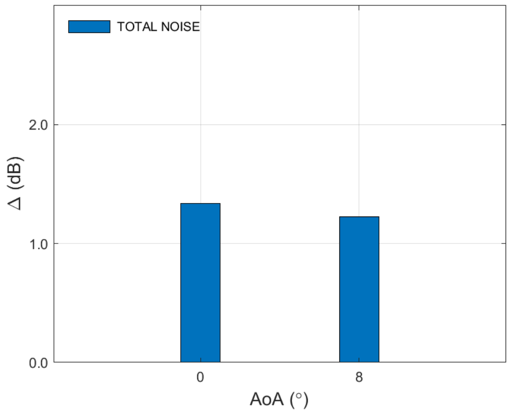

Figure 15. OASPL discrepancy with angle of attack (AoA) at nominal pitch.

Far-field Noise Directivity at non-zero AoA

When the AoA is different from zero, departures from the axisymmetric assumption of noise directivity are expected. Because loading in rotor blades exhibits changes while rotating - dependent with azimuthal angle. Consequently, directivity is examined at a sphere surface surrounding the open fan geometry. The spherical geometry has a radius equal to 10 forward rotor radius, $R = 10R_f$, and is centered around the intersection of the aft blade pitch axis and the axis of the open fan. Acoustic data are collected for a total of 1,334 acoustic receivers arranged along the polar direction with 36 receivers (5° separation) with 37 azimuthal arcs (10° separation). Definitions of the spherical coordinates are shown in Figure 16.

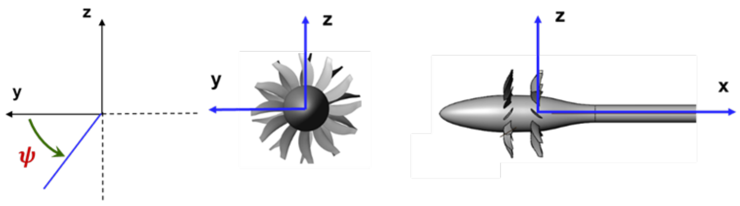

Figure 16. Spherical coordinate definition for CAA receivers.

Note: Geometry is a generic contrarotating open rotor and thus it is not the GE F31A31

The far-field noise directivity in terms of overall sound pressure level is shown in Figure 17 for the AoA = $8°$ case at corrected rotor speed of 6304 RPM. OASPL contours are shown at a spherical surface surrounding the F31/A31 open rotor model. The CAA predictions are achieved by means of the convective FW-H approach. OASPL contours exhibit lack of any axially symmetry, unlike cases at AoA = $0°$, in which axially symmetry is expected. Such three-dimensionality in the noise far-field results from the presence of crossflow in the plane of the rotors. Noise levels are larger in the lower hemisphere, i.e., at receivers with negative z coordinates, where the F31/A31 is tilted away from the flow. In contrast, low levels of noise are found in the upper hemisphere.

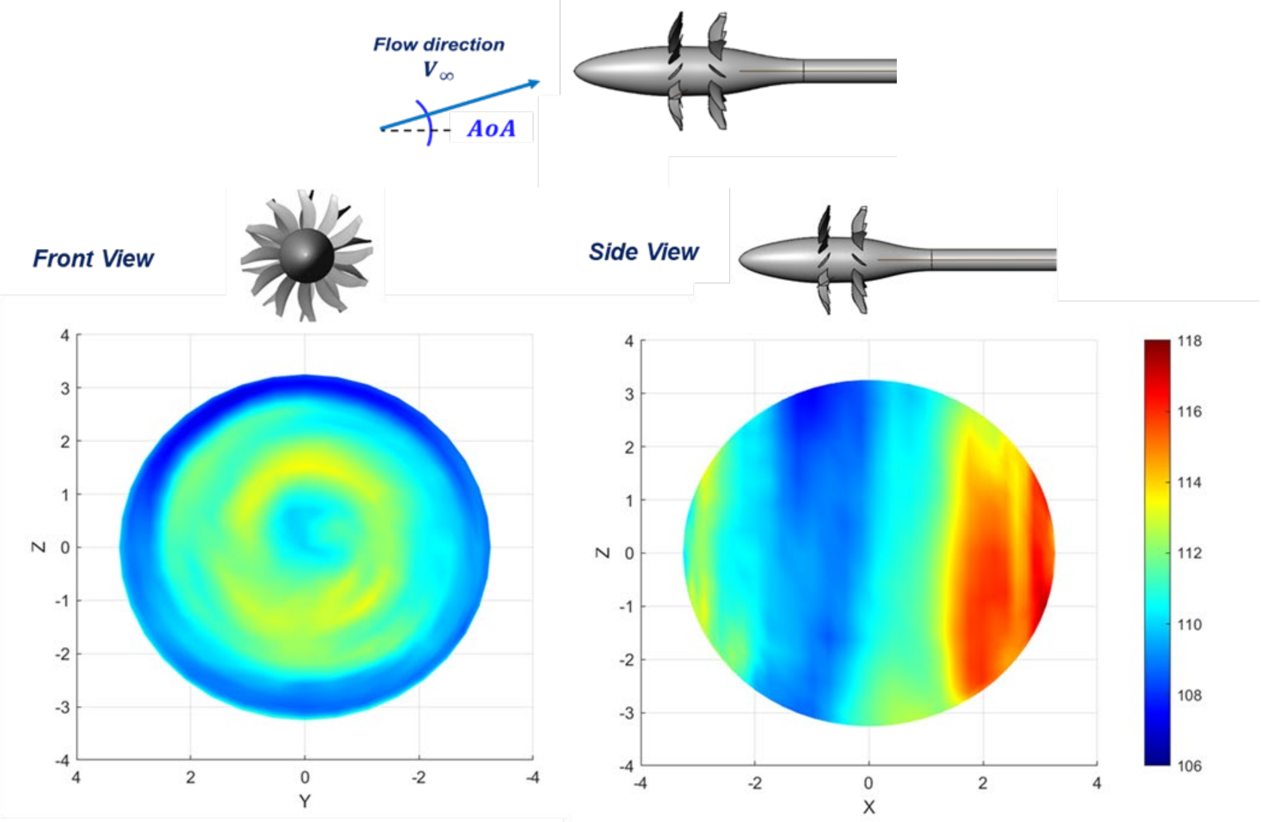

Figure 17. OASPL directivity at spherical surface for AoA = 8 ° case. Note: Geometry is a generic contrarotating open rotor and thus it is not the GE F31A31

A comparison of the directivity pattern between the non-zero and zero angle of attack cases are shown in Figure 18. The 2D contour plots are plotted in spherical angles. The contour on the left is the AoA = 0° case while the contour on the right is the AoA = 8° case. Note that in the former case axisymmetry is assumed – acoustics was predicted for a 180° arc rather than over the entire sphere. The lack of axial symmetry in the polar directivity is notorious for the non-zero-AoA case – OASPL directivity is different for different values of ψ. Lack of symmetry in the noise directivity results from the transverse component of the flow velocity. The existence of said component leads to periodic unsteady loading in the blades because of the variation in flow direction being ingested by the rotors. Such changes in flow direction exert changes in the local angle of attack experienced by the blades.

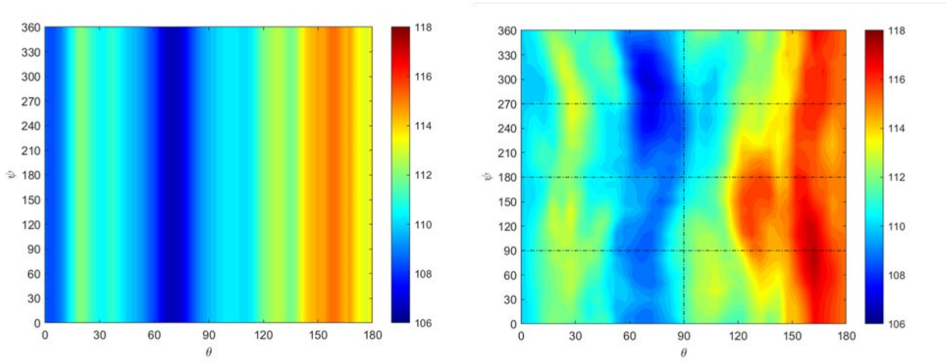

Figure 18. Total noise OASPL (dB) directivity in spherical coordinates: AoA = 0 ° case (left) and AoA = 8 ° case (right).

The OASPL directivity due to the noise component such as unsteady loading and thickness is shown in Figure 19 and Figure 20. These contours are similarly contrasted against the zero AoA case. It is noted that the directivity pattern of unsteady loading closely resembles that of total noise, suggesting that total noise is mostly dominated by it. The directivity pattern on thickness noise differs from that of the zero AoA case in that it exhibits a lack of axial symmetry. Moreover, a higher noise level is observed in the lower hemisphere compared with both the upper hemisphere and the zero AoA case.

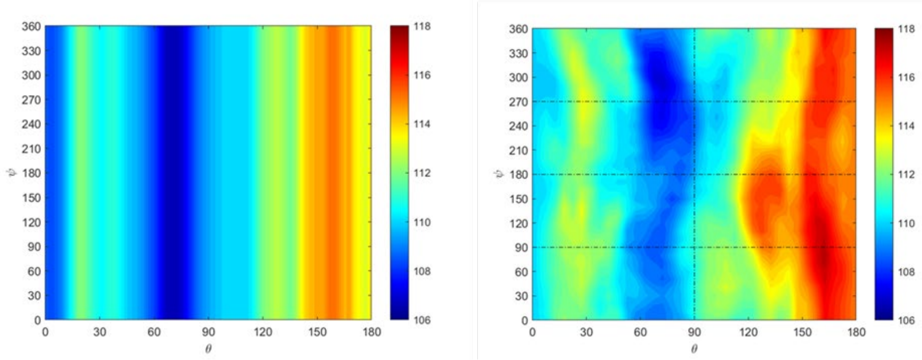

Figure 19. Unsteady loading OASPL in spherical coordinates: AoA = 0 ° case (left) and AoA = 8 ° case (right).

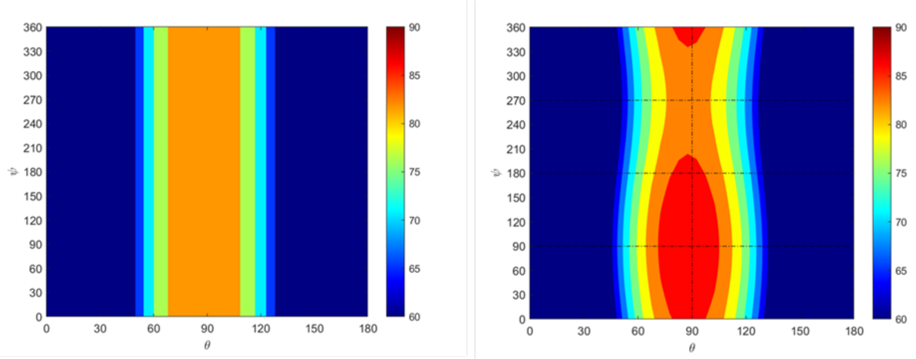

Figure 20. Thickness OASPL in spherical coordinates: AoA = 0° case (left) and AoA = 8° case (right).

Aerodynamics at non-zero AoA

In order to understand the unsteady loading that both rotors experience during operation at non-zero angle of attack flows, the axial force in one blade of each rotor is tracked as a function of both time and position. The latter is expressed by its azimuthal location. The blade starting position is approximately at the positive z-coordinate, $\psi = 0°$, and azimuth location is measured clockwise as shown in Figure 21.

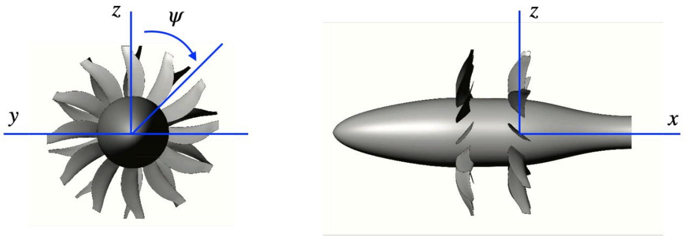

Figure 21. Azimuthal angle definition.

Note: Geometry is a generic contrarotating open rotor and thus it is not the GE F31A31.

The thrust time-variations in a single blade per rotor are shown in Figure 22 at angles of attack $\alpha_\infty = 0°$ and $8°$. Variations are shown as a function of both time and location. The latter is expressed by its azimuthal location. The starting position for both blades of the forward and aft rotor is at $\psi = 0°$, when their respective pitch axis aligns with the positive z-coordinate. A duration of four revolutions is shown for the unsteady thrust. For a non-zero AoA, the thrust pattern resembles a sinusoidal variation, and as a function of time, the thrusts in both blades seem to be close in phase. Such behavior is because both blades' starting position is at the same azimuthal location and both blades attain their largest value at approximately a quarter of their respective rotation. When the blade forces are plotted as a function of their azimuthal location, however, there is a phase shift of approximately $\pi/2$. This shift occurs because the maximum forces occur at $\pi/2$, whereas the minimum forces occur at $3\pi/2$ from their starting position following their respective direction in rotation. Note that because of the counter rotation in the aft rotor, maximum and minimum values instead occur at $3\pi/2$ and $\pi/2$, respectively. The degree of unsteadiness between the angle of attacks considered differs greatly. For $\alpha_\infty = 8°$, the amplitude approximately varies ± 40% over the time-averaged value, for $\alpha_\infty = 0°$, the amplitude is only approximately ±2.5 %.

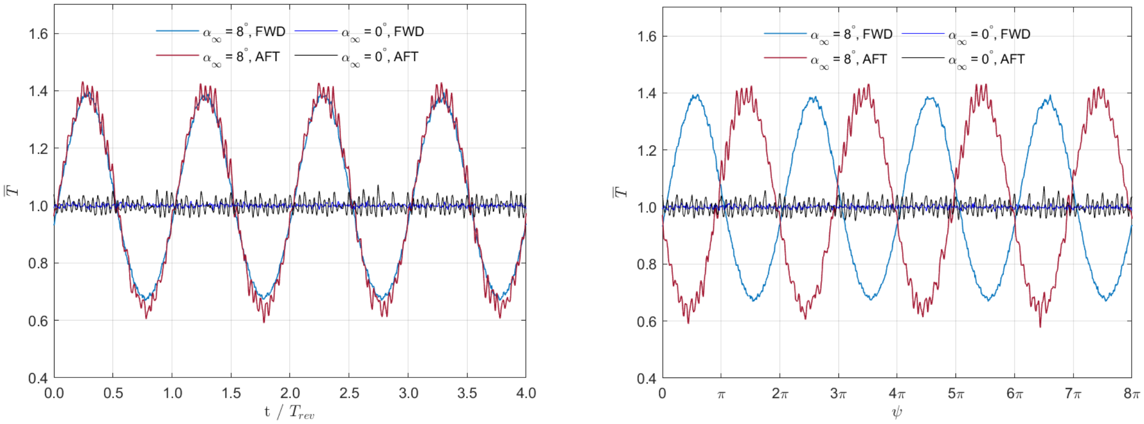

Figure 22. Thrust force normalized by the time-averaged value as a function of time (left) and azimuth (right).

The above behavior is due to the azimuthal dependence of loads in the blades occurring at a non-zero AoA. The tangential component of the flow, as seen from the moving blades, changes with azimuth; this in turn affects the angle of attack, thus leading to load dependence with azimuthal angle. In order to explain the azimuthal dependence, consider an idealized situation of a flow at non-zero angle of attack, in which the triangles of velocities as seen from two references of frames: an absolute one, which is fixed and aligned to the engine; and a relative frame, which rotates with the rotor, as shown in Figure 23. Moreover, while the absolute reference frame is a cartesian one $(x - y - z)$, the relative one is cylindrical $(r - \psi - x)$, while both having the axial coordinate x in common. From the fixed frame, velocities $\boldsymbol{c}$ are absolute; while from the rotating frame, velocities w are relative. Also, note that in the triangle of velocities, the only concern is with the projection of the absolute velocity onto the $\psi - x$ since the radial component is assumed not to have an effect in this idealized situation.

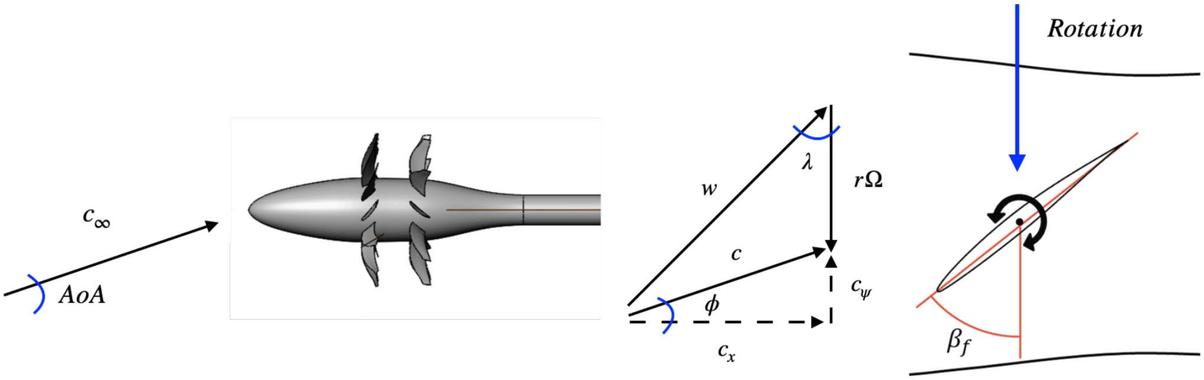

Figure 23. Flow angle in blades

Note: Geometry is a generic contrarotating open rotor and thus it is not the GE F31A31

The absolute velocity component in the $x - \psi$ plane can be expressed by the rotational and relative contribution, $\vec{c} = \overrightarrow{r\Omega} + \vec{w}$, where Ω is the blade angular speed. This velocity can also be decomposed into axial and tangential components, $\vec{c} = \overrightarrow{c_x} + \overrightarrow{c_\psi}$. The local blade AoA is measured from the relative velocity w with respect to the blade chord as follows:

$$\alpha = \gamma - \lambda,$$

where γ is the local chord angle and λ is the relative velocity angle. Note that the local angle of attack varies along the span of the blade since the chord angle depends on the value of the blade pitch angle as well as the twist angle at a particular radial location. As seeing in the triangle of velocities, the relative velocity orientation depends on its tangential component as follows:

$$\lambda = arctan\left(\frac{c_x}{w_\psi}\right),$$

which in turn depends on the projection of the absolute velocity in the tangential direction, $|w_\psi| = r\Omega \pm c_\psi$. Note that in the above equation, "+" applies when the tangential component of the absolute velocity c_ψ is against the movement of the blade and "-", when the movement is in the same direction as the blade movement. It follows that when the tangential flow is against the blade movement, the relative velocity angle decreases, whereas the angle increases when the tangential flow and blade movement coincide in direction. Note that in this idealized case, we have the following:

$$c_\psi = \ c_z\, sin(\psi) = c_\infty sin\,(AoA) \times \sin\,(\psi).$$

Consequently, the local angle of attack α increases with tangential flow against blade movement, whereas it decreases with flow in same blade movement direction. Note that $c_\psi = 0$ leads to a zero AoA case - the purely axial flow. Thus, examining the flow direction could help understand the blade sectional loading. The flow angle is then defined as:

$$\phi = arctan\left(\frac{c_\psi}{c_x}\right)$$

Note that the larger the tangential flow component respect to the axial component, the flow angle increases as well. Moreover, the sign of this angle depends on the direction of the azimuthal orientation and accordingly expresses the direction - against or in direction of blade movement. It is important to note that even though in an actual case the flow ingested by the rotor is more complicated – effects of nacelle and suction, the flow angle can still qualitatively provide insights into the azimuthal locations where the blade local angle is either low or high.

Instantaneous contours of flow angles upstream of the forward and aft rotor are shown in Figure 24, respectively. Note that these contours have been calculated by first transforming velocity components from a cartesian coordinate system, $x - y - z$, to a cylindrical coordinate system, $r - \psi - x$, where the x-direction is the same in both systems, but the transverse plane is expressed with polar components. Contours are plotted at transverse locations of 0.1m upstream of each rotor pitch axis. The flow angle ϕ upstream of the forward rotor are shown in Figure 24(a & b). At AoA = $0°$, the flow angle is small since although the flow is influenced by the nacelle, the ingested flow is mostly axial. Contrarily, at AoA = $8°$, the flow angle ϕ exhibits azimuthal dependence. On the left and right side, the flow angle exhibits negative and positive angles – angle is measured in the clockwise direction – with higher absolute values near $\pi/2$ and $3\pi/2$. In the bottom and upper sides - around 0 and π, the flow angles are, in contrast, small in absolute value, indicating negligible effects of tangential components with the flow being mostly radial, which might be attributed to the normal direction of the flow to the blade movement and the effect of the nacelle on the incoming flow. Also, larger flow angles, in absolute values, result on regions that are either favorable, around $\pi/2$, since the blade movement is against the tangential component of the flow; and unfavorable region, around $3\pi/2$, due to tangential components in the direction of rotation, respectively. Moreover, note that these azimuthal locations of favorable and unfavorable flow correspond to the maximum and lowest values of the axial force at azimuthal locations of $\pi/2$ and $3\pi/2$, respectively, as previously shown in Figure 22.

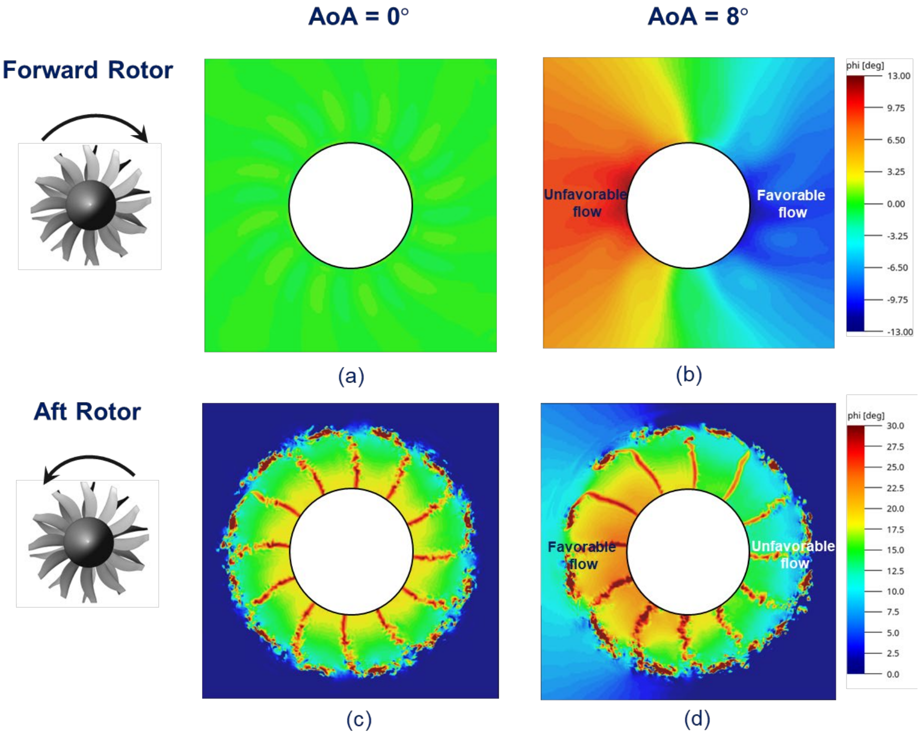

Figure 24. Flow angle (ϕ) upstream of forward rotor (a -b) aft rotor (c-d) **Note: Geometry is a generic contrarotating open rotor and thus it is not the GE F31A31**

The flow angle ϕ upstream of the aft rotors is shown in transverse planes in Figure 24(c & d). This inter-rotor flow exhibits flow angles that are fairly periodic for the AoA = $0°$ case. The wakes as well as the flow structures due to the tip vortices from the forward rotor blades are quite apparent. In thee AoA = $8°$ case, on the other hand, the flow angle is azimuth dependent. Indeed, regions of larger flow angles are developed on the left side, around $3\pi/2$, whereas smaller flow angles are observed on the right side, around $\pi/2$. The region with larger flow angles leads to more favorable flow since the tangential component acts against the aft rotation, which in turn increases the local angle of attack, increasing loads in blades. On the contrary, the region on the right with smaller flow angles creates relatively smaller tangential components compared to the other region and that of the AoA = $0°$ case. Consequently, the local angle of attacks would be smaller than those of the region of favorable flow. Note also that the azimuthal locations of favorable and unfavorable flow correspond to the maximum and lowest values of the axial force at azimuthal locations of $3\pi/2$ and $\pi/2$, respectively, as previously shown in Figure 22.

Considerations

The results reported in this document should be understood given the following considerations:

1. Lack of knowledge regarding actual geometry
    - Variability in installation of the F31/A31 wind tunnel model such as blade pitch variation could lead to angular variation of up to 0.1 ° from blade to blade.
    - Blade deformation due to rotation – blades deform differently at every rotor speeds.
2. Simulation aspects
    - The FW-H solver with impermeable surfaces used for CAA simulations with calibrated pitch angle does not account for convection effects [13].
    - Impermeable surfaces may not account for very near effects in the flowfield.

Note that all of the above can influence simulation predictions and can hence result in discrepancies, although the magnitude of such discrepancies is unknown. Installation variability has been argued to result in discrepancies in both aerodynamics and acoustics [8,9]. Moreover, not accounting for deformation due to operating conditions has also been found to result in aerodynamic and acoustic discrepancies [9].

Conclusions

A numerical study was carried out for validating a sub-set of the experimental cases of the open fan configuration based on the F31/A31 blades. Specifically, the focus is on the low-speed cases with NTO pitch settings. Aerodynamic calibration is carried out prior to acoustic validation. The numerical simulations rely on a hybrid approach. The unsteady aerodynamic flowfield is obtained by explicitly solving the transient and compressible lattice-Boltzmann equations, implemented on a commercial LBM solver. The far-field aeroacoustics is predicted by a FW-H solver, which employs transient flow data recorded at impermeable surfaces. Aeroacoustic validations are carried out with simulations using said calibrated pitch settings. The aerodynamic calibration is based on minimizing thrust discrepancy between experimental and numerical values. Such criterion is chosen because loading noise is of relevance to the conditions of interest. Results of calibration are to slightly increase the pitch angles in both rotors. The effects on aeroacoustics is to slightly increase overall noise metrics. Such increment is due to the increase in thrust given the slightly larger pitch angles on the calibrated case. The far-field aeroacoustics using the calibrated pitch settings results in a decreasing trend for the measurements of discrepancy in overall noise metrics with rotor speed. OASPL discrepancy decreases from 2.5 to 1.6 dB. The overall acoustic power follows a similar trend with the discrepancies of 2.5 and 0.36 dB, found at the lowest and highest rotor speed, respectively. Among the cases investigated at non-zero angle of attack, OASPL discrepancies no larger than 2.0 dB are found. Closer examination of the farfield noise results in a noticeable lack of axisymmetry. Higher noise levels are found in the lower hemisphere, where the open rotor is tilted away. Finally, comparisons with simulations with nominal pitch settings show that calibration increases discrepancies. Such an outcome could be attributed to the fact that simulations of nominal pitch cases exhibit lower thrust values compared to experiments. Aerodynamic calibration results on slightly larger pitch angles, which in turn increase thrust and consequently noise levels.

Milestone(s)

None.

Major Accomplishments

Regarding extended validation, all cases at zero angle of attack have been completed.

Publications

- “Aerodynamic Calibration for Aeroacoustics Validation of an Open Fan Configuration,” in AIAA SciTech 2023

Outreach Efforts

None.

Awards

None.

Student Involvement

For this task, Brenton Willier (continuing PhD student with U.S. person credentials) and Grant Stevenson (continuing MS student with U.S. person credentials) worked on geometry preparation for numerical analysis and analysis of acoustic data.

Plans for Next Period

None.

References

[1] Stephens, D. B., “Data Summary Report for the Open Rotor Propulsion Rig Equipped with F31/A31 Rotor Blades,” NASA/TM-2014-216676, 2014.

[2] Sree, D., “Far-Field Acoustic Power Level and Performance Analyses of F31/A31 Open Rotor Model at Simulated Scaled Takeoff, Nominal Takeoff, and Approach Conditions: Technical Report I,” NASA/CR-2015-218716, 2015.

[3] Sree, D., “Near-Field Acoustic Power Level Analyses of F31/A31 Open Rotor Model at Simulated Cruise Conditions: Technical Report II,” NASA/CR-2015-218845, 2015.

[4] Elliot, D. M., “Initial Investigation of the Acoustics of a Counter-Rotating Open Rotor Model with Historical Baseline Blades in a Low-Speed Wind Tunnel,” NASA/TM-2012-217258, 2012.

[5] “Acoustical Society of America: Method for Calculation of the Absorption of Sound by the Atmosphere,” ANSI S1.26-1995, 1995.

[6] Rizzi, S. A., Stephens, D. B., Berton, J. J., Zante, D. E. V., Wojno, J. P., and Goerig, T. W., “Auralization of FlyoverNoise from Open-Rotor Engines Using Model-Scale Test Data,” Journal of Aircraft, Vol. 53, No. 1, 2016, pp. 117–128.

[7] Hubbard, H. H., “Aeroacoustics of Flight Vehicles: Theory and Practice,” NASA/TR-90-3052, 1991.

[8] Envia, E., “Open Rotor Aeroacoustic Modeling,” NASA TM 2012-217740, 2012.

[9] Falissard, F., Boisard, R., Gaveriaux, R., Delattre, G., Gardarein, P., Chelius, A., Canard-Caruana, S., and Mauffrey, Y., “Influence of Blade Deformations on Open-Rotor Low-Speed and High-Speed Aerodynamics and Aeroacoustics,” Journal of Aircraft, Vol. 55, No. 6, 2018, pp. 2267–2281.

[10] Casalino, D., Hazir, A., and Mann, A., “Turbofan Broadband Noise Prediction Using the Lattice Boltzmann Method,” AIAA Journal, Vol. 56, No. 2, 2018, pp. 609–628.

[11] Romani, G., QingQing, Y., Avallone, F., Ragni, D., and Casalino, D., “Numerical Analysis of fan noise for the NOVA boundary-layer ingestion,” Aerospace Science and Technology, Vol. 96, 2020.

[12] Nark, D. M., Jones, W. T., Boyd, D. D., and Zawodny, N. S., “Isolated Open Rotor Noise Prediction Assessment Using the F31A31 Historical Blade Set,” AIAA paper 2016-1271, San Diego, CA, 2016.

[13] Cerizza, D., DS Simulia corporation, private communication, 2022.

[14] L. S. Langston, "Open Rotor Engines—Still an Open Question?," *ASME. Mechanical Engineering.* , December 2018.

[15] SAFRAN-GROUP, "Safran celebrates successful start of Open Rotor demonstrator tests on new open-air test rig in southern France," October 2017. [Online]. Available: https://www.safran-group.com/media/safran-celebrates-successful-start-open-rotor-demonstrator-tests-new-open-air-test-rig-southern-france-20171003.

[16] Smithsonian National Air and Space Museum, "General Electric GE36 Unducted Fan (UDF) Turboprop Engine," [Online]. Available: https://airandspace.si.edu/collection-objects/general-electric-ge36-unducted-fan-udf-turboprop-engine/nasm_A19920001000.

[17] FAA, General Electric, "Open Rotor Engine Aeroacoustic Technology Final Report," 2014.

[18] M. McCarthy, "Contra-rotating Open Rotor Reverse Thrust Aerodynamics," Cranfield University, 2011.

[19] NoiseNews, "Tonal Noise Analysis with Optimus Green Sound Level Meters," 2017.

[20] S. Glegg and W. Devenport, Aeroacoustics of Low Mach Number Flows, Vols. Chapter 16 - Open rotor noise, 2017, pp. 399-436.

[21] KAIST Aeroacoustics Lab, "Flow and Acoustics of Turbo Jet and Rocket," [Online]. Available: https://sites.google.com/site/aeac1234/applications/hydraulic-power.

[22] FAA, General Electric, "Open Rotor Engine Aeroacoustic Technology Final Report," 2014.

[23] J.-S. Jang, S. Choi, H.-I. Kwon, D.-K. Im, D.-J. Lee and J.-H. Kwon, "A Preliminary Study of Open Rotor Desing Using a Harmonic Balance Method," in *50th AIAA Aerospace Sciences Meeting Including the Horizons Forum and Aerospace Exposition*, 2012.

[24] H. Kwon, S. Choi, J.-H. Kwon and D. Lee, "Surrogate-Based Robust Optimization and Design to Unsteady Low-Noise Open Rotors," *Journal of Aircraft,* 2016.

[25] D. A. Smith, A. Filippone and N. Bodjo, "A Parametric Study of Open Rotor Noise," in *25th AIAA/CAES Aeroacoustics Conference*, 2019.

[26] S. Yi, H.-I. Kwon, D. Im, S. Choi, M. Park and D.-J. Lee, "Parameter Study of Low Noise CROR System," in *34th AIAA Applied Aerodynamics Conference*, 2016.

[27] H.-I. Kwon, S.-g. Yi, S. Choi, D.-J. Lee, J.-H. Kwon and D.-K. Im, "Design of a Low-Noise Open Rotor Using an Implicit Harmonic Balance Method," in *51st AIAA Aerospace Sciences Meeting*, 2013.

[28] R. Schnell, J. Yin, C. Voss and E. Nicke, "Assessment and Optimization of the Aerodynamic and Acoustic Characteristics of a Counter Rotating Open Rotor," in *ASME Turbo Expo*, 2010.

[29] B. A. Janardan and P. R. Gliebe, "Acoustic characteristics of counterrotating unducted fans from modelscale tests," *Journal of aircraft,* vol. 27, no. 3, 1990.

[30] P. A. Moshkov, V. Samokhin and A. Yakovlev, "Problem of the Community Noise Reduction for Aircraft with Open Rotor Engines," *Russian Aeronautics Vol. 61 No. 4,* pp. 647-650, 2018.

[31] B. Shivashankara, D. Johnson and R. Cuthbertson, "Installation Effection on Counter Rotation Propeller Noise," *AIAA,* 1990.

[32] J. Ricouard, E. Julliard and et al, "Installation effects on contra-rotating open rotor noise," *16th AIAA/CEAS aeroacoustics conference,* 2010.

[33] A. Stuermer and Y. Jianping, "Aerodynamic and aeroacoustic installation effects for pusher-configuration CROR propulsion systems," *28th AIAA Applied Aerodynamics Conference,* 2010.

[34] T. Sinnige and L. L. M. Veldhuis, "Pylon Trailing Edge Blowing Effects on the Performance and Noise Production of a Pusher Propeller," 2014.

[35] R. W. Harris and R. Cuthbertson, "UDF/727 Flight Test Program," in *AIAA/SAE/ASME/ASEE 23rd Joint Propulsion Conference*, San Diego, CA, 1987.

[36] H. Nichols, "UDF engine/MD80 flight test program," in *AIAA/SAE/ASME/ASEE 24th Joint Propulsion Conference*, Boston, Mass., 1988.

[37] J. Dansie, "What should my tail look like?," HMFC, 2018. [Online]. Available: http://www.hmfc.com.au/index.php/ground-school/what-should-my-tail-look-like. [Accessed 07 2021].

[38] J. Kennedy, P. Eret and G. Bennett, "A parametric study of airframe effects on the noise emission from installed contra-rotating open rotors," *International Journal of Aeroacoustics,* 2018.

[39] L. Sanders, D. C. Mincu, P. L. Vitagliano, M. Minervino, J. Kennedy and G. Bennett, "Prediction of the acoustic shielding by aircraft empennage for contra-rotating open rotors," *International Journal of Aeroacoustics,* pp. 626-648, 2017.

[40] J. Kennedy, P. Eret and G. Bennett, "A parametric study of installed counter rotating open rotors," in *19th AIAA/CEAS Aeroacoustics Conference*, Berlin, Germany, 2013.

[41] L. Dürrwächter, M. Keßler and E. Krämer, "Numerical Assessment of Open-Rotor Noise Shielding with a Coupled Approach," *AIAA Journal,* pp. 57(5), 1930-1940, 2019.

[42] M. Czech and R. H. Thomas, "Open Rotor Installed Aeroacoustic Testing with Conventional and Unconventional Airframes," in *19th AIAA/CEAS Aeroacoustics Conference*, Berlin, Germany, 2013.

[43] D. B. Stephens and E. Envia, "Acoustic Shielding for a Model Scale Counter-rotation Open Rotor," in *17th AIAA/CEAS Aeroacoustics Conference*, 2011.

[44] J. Berton, "Empennage Noise Shielding Benefits for an Open Rotor Transport," in *17th AIAA/CEAS Aeroacoustics Conference (32nd AIAA Aeroacoustics Conference)*, Portland, Oregon, 2011.